

Light-trapping by wave interference in intermediate-thickness silicon solar cells

SAYAK BHATTACHARYA^{1,*}  AND SAJEEV JOHN²

¹Dept. of Electronics & Communication Engineering, Indraprastha Institute of Information Technology Delhi, New Delhi 110020, India

²Dept. of Physics, University of Toronto, 60 St. George Street, Toronto M5S 1A7, Ontario, Canada

*sayak@iitd.ac.in

Abstract: The power conversion efficiency of crystalline silicon (*c-Si*) solar cells have witnessed a 2.1% increase over the last 25 years due to improved carrier transport. Recently, the conversion efficiency of *c-Si* cell has reached 27.1% but falls well below the Shockley-Queisser limit as well as the statistical ray-optics based 29.43% limit. Further improvement of conversion efficiency requires reconsideration of traditional ray-trapping strategies for sunlight absorption. Wave-interference based light-trapping in photonic crystals (PhC) provides the opportunity to break the ray-optics based $4n^2$ limit and offers the possibility of conversion efficiencies beyond 29.43% in *c-Si* cells. Using finite difference time domain simulations of Maxwell's equations, we demonstrate photo-current densities above the $4n^2$ limit in 50 – 300 μm -thick inverted pyramid silicon PhCs, with lattice constant 3.1 μm . Our 150 μm -thick PhC design yields a maximum achievable photo-current density (MAPD) of 45.22 mA/cm^2 . We consider anti-reflection coatings and surface passivation consisting of $\text{SiO}_2 - \text{SiN}_x - \text{Al}_2\text{O}_3$ stacks. Our design optimization shows that a 80 – 120 – 150 nm stack leads to slightly better solar light trapping in photonic crystal cells with thicknesses <50 μm , whereas the 80 – 40 – 20 nm stack performs better for cells with thicknesses >100 μm . We show that replacing SiN_x with SiC may improve the MAPD for PhC cells thinner than 100 μm . For a fixed lattice constant of 3.1 μm , we find no significant improvement in the solar absorption for 50 and 100 μm -thick cells relative to a 15 μm cell. A substantial improvement in the MAPD is observed for the 150 μm cell, but there is practically no improvement in the solar light absorption beyond 150 μm thickness.

© 2024 Optica Publishing Group under the terms of the [Optica Open Access Publishing Agreement](#)

1. Introduction

The need for clean, efficient and cost-effective energy has motivated the quest for high-efficiency photovoltaic technologies. Direct bandgap semiconductor based solar cells, with high sunlight absorption, are a popular choice for thin-film photovoltaic technologies. The current record efficiencies of single junction thin-film photovoltaics range between 22 – 29.1%. *CdTe*, *CIGS*, Perovskite and *GaAs* have shown power conversion efficiencies of 22.3%, 23.6%, 26% and 29.17% respectively [1]. As of now, the conversion efficiencies in *CdTe* and *CIGS* fall well below than that of crystalline silicon (*c-Si*) cells. In addition, the toxicity of *Cd*, the scarcity of *Te*, the slow and expensive production of *CIGS*, the lack of stability of perovskites, and the cost of *GaAs* pose obstacles to their widespread use [2–4].

Crystalline silicon (*c-Si*) and polycrystalline silicon, despite being indirect bandgap semiconductors, are the most widely used materials for solar cells, with above 90% market share. Silicon is the second most abundant material by mass (after oxygen) in the earth's crust. In addition to its abundance, silicon is non-toxic and benefits from mature fabrication technologies. The ability of *c-Si* solar cells to achieve >25% conversion efficiency is well-established. However, the indirect bandgap of *c-Si* red has required that silicon solar cells be made hundreds of microns thick in order to capture sufficient sunlight. Some of the best *c-Si* cells, such as UNSW PERL cell with 25% efficiency [5,6], ISFH POLO interdigitated back contact (IBC) cell with 26.1%

efficiency [7,8], Kaneka heterojunction IBC cell with 26.7% efficiency [9] and the Longi Solar heterojunction IBC cell with 26.81% efficiency [10] have thicknesses of 400, 290, 165 and 130 μm , respectively. One possible cause of improved open-circuit voltage (V_{OC}) with decreased thickness is the reduction in bulk recombination losses. This is evident from the steadily increasing V_{OC} of the four cells with decreasing thickness: 0.706, 0.7266, 0.738 and 0.7514V, respectively [11]. While, the V_{OC} has improved by $\sim 50\text{mV}$ over the last 2 decades, the best short-circuit current densities (J_{SC}) have remained in the range of 42.2 to 42.65 mA/cm^2 . The J_{SC} values of the Kaneka IBC cell and the ISFH POLO-IBC cell are 42.65 and 42.62 mA/cm^2 , respectively. Despite this similarity, the latter is 125 μm thicker than the former. The UNSW PERL cell, although the thickest, exhibits a lower J_{SC} of 42.2 mA/cm^2 due to the shading loss from the front contacts. In the thinner cell, with 26.81% efficiency, by Longi Solar, the V_{OC} improves by 13.4 mV but the J_{SC} exhibits a sharp drop to 41.45 mA/cm^2 . The recent cell of Longi Solar, with a record efficiency of 27.1%, has a slightly smaller V_{OC} of 0.7425V and an improved J_{SC} of 42.61 mA/cm^2 in comparison to its counterpart with 26.81% efficiency [11].

Traditional $c - Si$ cells have been designed using ray-optics concepts to trap sunlight. The front surfaces of the cells are sometimes randomly textured or have feature sizes much larger than the wavelength of the light. Traditional ray-trapping appears to be close to saturation for sunlight capture as evidenced by a comparison between the POLO-IBC and Kaneka IBC cells. Comparing the Kaneka and the Longi cells suggests that efficiency boosting by V_{OC} , using a thinner cell, would lead (in ray optics) to diminished light-trapping, providing only marginal efficiency improvement.

Statistical ray-optics imposes a putative upper limit on solar absorption in traditional cells, known as the $4n^2$ (Lambertian) limit [12], where n is the real part of the refractive index of the absorber. This hypothesized limit involves the unrealistic assumptions of no specular reflection from the top surface of the cell and the complete absence of wave-interference effects within the cell. Solar absorption in existing $c - Si$ cells falls well below the $4n^2$ limit. In practice, it has not been possible so far to achieve a $4n^2L$ path-length over the 300 – 1200 nm spectral range using a physical ray-trapping texture on the surface of a slab of thickness L . Experimentally, it has been possible to achieve close to Lambertian light absorption in the 400 – 1200 nm wavelength range [13]. However, the assumption of no specular reflection is particularly unrealistic at wavelengths shorter than 400 nm where $n \approx 6$. In any event, the $4n^2$ limit would imply a conversion efficiency of the $c - Si$ cells restricted to well below 29.43% [14] when the practical realities such as Shockley-Read-Hall recombination, surface recombination, and non-zero reflectance of the front surface of the cells are included.

Wave-interference based light-trapping in photonic crystals (PhC) [15,16] provides a new paradigm for solar absorption [17–19] beyond the $4n^2$ limit. Coupled optical and electronic optimizations of thin-film PhC solar cells [17,18,20], taking into account experimentally feasible doping profiles, bulk recombination life-times and surface passivation, have shown that the single-junction $c - Si$ cells can potentially achieve conversion efficiencies of 30%. Silicon thin-film PhCs with unit cells in the form of nano-wires, vertical and slanted conical pores, inverted pyramids, and slanted parabolic pores have been theoretically optimized for solar light absorption and in some cases fabricated [19,21–42]. Detailed finite difference time domain (FDTD) simulations of Maxwell's equations have shown that conical-pore [19], parabolic pore [42] and inverted pyramid PhCs [17,18,20] can break the $4n^2$ limit of light-trapping in 1 – 15 μm -thick $c - Si$ cells. PhCs consisting of pore arrays can be fabricated by dry-etching. However, without post-treatment by wet-etching, the surface recombination velocity would be very high and offset the advantages of wave-interference-based light-trapping. Inverted pyramid $c - Si$ PhCs can be fabricated by *KOH* wet-etching alone and typically do not require major post-treatment to remove extensive electronic defects induced by etching. The ability of parabolic pore and inverted pyramid PhCs to break the $4n^2$ limit has been confirmed by subsequent experiments [43].

The lattice constant and feature sizes in the relevant photonic crystals are typically on the order of (or slightly greater than) the wavelength of light. The resulting wave-interference-based light-trapping requires accurate numerical solutions of Maxwell's equations. In the statistical ray-optics picture, the incoming rays are scattered by the textured front surface of the absorber according to a Lambertian probability distribution, $f(\theta) = \frac{1}{\pi} \cos(\theta)$ for $0 \leq \theta \leq \frac{\pi}{2}$, θ being the scattering angle with respect to the surface normal. This implies, the probability that the rays are scattered further away from the surface normal (i.e. with higher values of θ) is low and it is impossible for the light to travel along a direction parallel to the surface. In contrast, the flow of light inside the PhC is far richer than the simplistic assumptions of ray-optics. PhCs can give rise to parallel to interface refraction (PIR) that redirects light nearly parallel to the interface [44]. Wave-interference effects lead to very closely spaced resonances arising from slow-light modes and vortex-like light-flow patterns [17,19,42]. This rich variety of optical phenomena are outside the realm of ray-optics. The slow-light modes increase the dwell-time of the photons inside a thin-film $c - Si$ PhC cell well beyond the predictions of traditional ray-trapping concepts. This longer dwell-time leads to higher solar light absorption in $10 - 15 \mu m$ -thick $c - Si$ PhCs, than observed in cells that are several hundreds of microns thick. Wave-interference-based light-trapping in thin-film $c - Si$ PhCs proffers power conversion efficiencies even slightly beyond 30% [18]. This is the result of significant increase in V_{OC} due to reduced bulk-recombination, while simultaneously attaining high J_{SC} through the wave nature of light [17,18].

Improved solar light-trapping is the key to boosting efficiencies of state-of-the-art $c - Si$ cells. Although PhCs have revealed unprecedented light absorption over the $300 - 1200 nm$ wavelength range in thin $1 - 20 \mu m$ $c - Si$ cells, the potential for wave-interference-based light trapping in intermediate-thickness $c - Si$ cells has not been fully explored. In this article, we analyze the light-trapping performance of $10 - 300 \mu m$ -thick $c - Si$ inverted pyramid PhCs incorporating established, passivating, anti-reflection coatings (ARC). We perform precise 3D FDTD simulations of Maxwell's equations for cell-thickness greater than $50 \mu m$. To our knowledge, intensive FDTD simulations have not been performed previously for $50 - 300 \mu m$ -thick cells.

Due to very long computational runtime of the $50 - 300 \mu m$ -thick PhC cells, we optimize the ARCs on thinner cells and use the same ARCs in the thicker cells. Optimization of lattice constants of thick PhCs is also time-consuming. Instead, we optimize ARC layers, for a fixed lattice constant of $3.1 \mu m$. This architecture was shown previously to maximize the solar absorption in $15 \mu m$ -thick PhC cells [17,20] and is easier to fabricate than those with smaller lattice constant. While further optimization of the lattice constant may improve the light trapping for intermediate thickness solar cells, the results presented below provide a useful lower bound on predicted performance.

Here, we provide a brief overview of our results. We consider the 3-layer ARC comprising of $SiO_2 - SiN_x - Al_2O_3$, with proven passivation in the high efficiency POLO cells [7,8]. Our simulations show that a large variety of PhC cells with optimized ARC configurations provide solar light absorption beyond the $4n^2$ limit. For the fixed lattice constant of $3.1 \mu m$, we find no improvement in solar absorption in $50 - 100 \mu m$ -thick PhC cells in comparison to the $15 \mu m$ PhC cell. Our ARC optimization also shows that while the previously used [7,8] $80 - 40 - 20 nm$ stack of $SiO_2 - SiN_x - Al_2O_3$ ARC is optimum for PhC cells thicker than $100 \mu m$, a $80 - 120 - 150 nm$ stack exhibits better light-trapping in PhC cells thinner than $100 \mu m$. Replacement of SiN_x with higher refractive-index SiC ($n = 2.6$), improves light-trapping in PhC cells thinner than $100 \mu m$. Our $150 \mu m$ -thick PhC cell (using SiC) exhibits a maximum achievable photo-current density (MAPD) of $45.22 mA/cm^2$, surpassing the $4n^2$ limit. This is well beyond the measured photo-current density of any laboratory $c - Si$ cell. As the cell thickness is increased beyond $150 \mu m$, there is practically no improvement of MAPD. This suggests that cells thicker than $150 \mu m$, with lattice constant $3.1 \mu m$, yield only increased the bulk-recombination loss, decreased

V_{OC} , and lower conversion efficiency. Inverted pyramid PhCs are readily fabricated on the surface of 50 – 150 μm -thick cells [43,45–47]. Combined with state-of-the-art electronics utilized in $c - \text{Si}$ cells, wave-interference-based light-trapping may provide higher efficiency $c - \text{Si}$ solar cells over a broad range of thicknesses.

2. Inverted pyramid photonic crystal cell architecture and numerical method

Figure 1(a) depicts the architecture of an IBC solar cell, with inverted pyramid PhC texture at the front surface. The pyramids have a side-wall angle of 54.7° . This is achieved by mask-assisted etching of the (100) surface of a $c - \text{Si}$ wafer by either “wet” KOH etch or “dry” reactive ion (plasma) etch [45–47], exposing the (111) surfaces. We assume a lattice constant of $a = 3.1 \mu\text{m}$ and a mesa (flat region between the edges of two consecutive inverted pyramids) width, b , of 30nm in all our computations. While a time-consuming optimization of lattice constant for each cell thickness may lead to slight further improvement in MAPD, we use the above architecture to establish an important lower bound on potential performance. The anti-reflection layer at the front surface of the PhC-IBC cell consists of a stack of 3 dielectrics with refractive indices n_i , $i = 1, 2, 3$. Throughout this article, an $h_1 - h_2 - h_3$ ARC represents a 3-stack ARC, where h_i represents the conformal thickness (in nm) of the dielectric layer of refractive index n_i . $i = 3$ represents the dielectric layer coated right on the $c - \text{Si}$ surface, $i = 2$ refers to the middle dielectric layer of the stack and $i = 1$ is the top most layer. In all our simulations, $i = 3$ corresponds to Al_2O_3 , which also has a demonstrated [7,8] surface passivation effect by producing a front-surface electric field within the silicon below. For example, a 80 – 40 – 20 ARC of SiO_2 - SiN_x - Al_2O_3 represents a 3-layer ARC of 20nm of Al_2O_3 ($n_3 = 1.77$) on the silicon surface, 40nm of SiN_x ($n_2 = 1.9$) on top of Al_2O_3 and 80nm of SiO_2 ($n_1 = 1.47$) on top of SiN_x . Figure 1(b) depicts the unit cell of the PhC with anti-reflection coatings (not shown). For optical simulations, the interdigitated back contacts are modeled as a perfect electrical conductor (PEC) underneath the $c - \text{Si}$ bulk. We assume that the required small gap between the adjacent contacts is optically insignificant. The thickness, H , of the $c - \text{Si}$ bulk varies between 10 – 300 μm . We assume periodic boundary conditions along x and y - directions. The boundaries of the computation domain, parallel to the xy -plane are terminated with perfectly matched layers (PML).

The numerical simulations are performed using an open-source package, Electromagnetic Template Library (EMTL) [48,49] that supports parallel processing and solves Maxwell’s equations through accurate implementation of finite difference time domain (FDTD) technique. For 10 and 15 μm -thick cells, we use a spatial resolution of $\Delta x = \Delta y = \Delta z = 20\text{nm}$ for all wavelengths. Here Δx , Δy and Δz denote the spatial resolution along x , y and z -axis, respectively. For 50 – 300 μm -thick cells, we use $\Delta x = \Delta y = \Delta z = 20\text{nm}$ and 30nm for 300 – 550nm and 550 – 1200nm wavelength ranges, respectively. In all cases we ensure the stability of the solutions through a Courant factor $S \leq \frac{1}{\sqrt{3}}$ [50].

In our FDTD computations, the structure is illuminated with a spatially uniform broad-band optical pulse. Since it is difficult to achieve numerical convergence over the entire 300 – 1200nm wavelength range in a single FDTD simulation, we perform two separate FDTD simulations corresponding to the shorter and longer wavelengths. Accurate modeling of the dispersion of $c - \text{Si}$ is crucial in order to ensure correct absorption in the solar cell. We model the dispersion of $c - \text{Si}$ over the 300 – 1000nm wavelength range using the fitting parameters for a modified Lorentz model, described earlier [51]. The dispersion model corresponding to 1000 – 1200nm wavelength range is described more explicitly in Appendix A. In our FDTD computations, flux planes above and below the structure record the wavelength dependent reflection $R(\lambda)$ and transmission $T(\lambda)$. From these, the wavelength dependent absorption $A(\lambda)$ is calculated as:

$$A(\lambda) = 1 - R(\lambda) - T(\lambda) \quad (1)$$

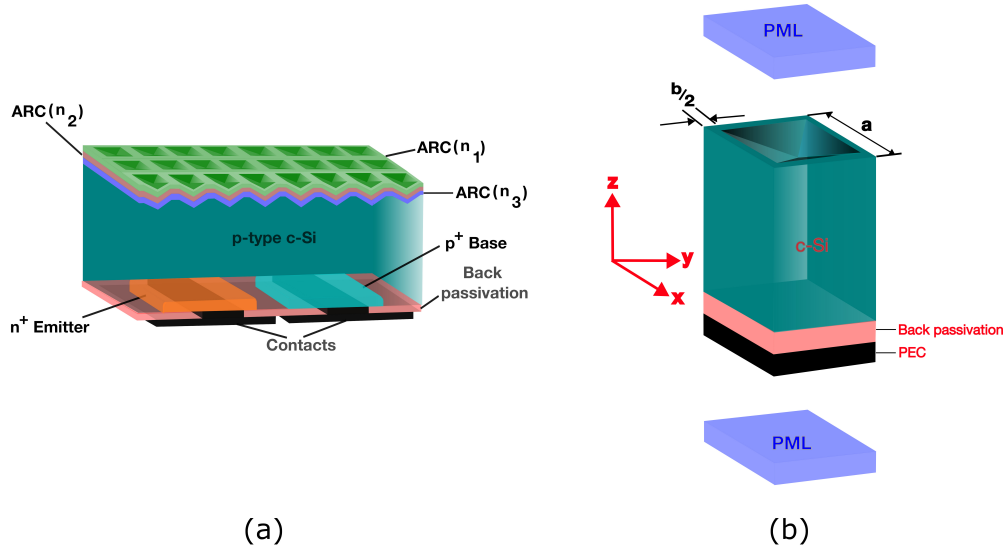


Fig. 1. Inverted pyramid photonic crystal solar cell architecture. ARC (n_3) consisting of Al_2O_3 is assumed to provide a passivating front surface field. (a) Interdigitated back-contact cell with a 3-layer anti-reflection coating. (b) Optically equivalent inverted pyramid unit cell used for numerical simulations. For clarity, the 3 layer anti-reflection coating at the top of the cell is not shown. The photonic crystal has lattice constant $a = 3.1\mu m$ and mesa $b = 30nm$. We apply periodic boundary conditions along x and y -directions. The computation cell boundaries parallel to the xy -plane are terminated with perfectly matched layers.

We calculate the MAPD over a wavelength range $[\lambda_1, \lambda_2]$ as:

$$J_{MAPD} = \int_{\lambda_1}^{\lambda_2} \frac{e\lambda}{hc} I(\lambda) A(\lambda) d\lambda \quad (2)$$

where, $I(\lambda)$ represents the *AM1.5G* spectrum.

3. Thin silicon inverted pyramid photonic crystal cells

Wave-interference-based light-trapping in PhC solar cells cannot be modeled using ray-tracing. Wave phenomena, such as parallel-to-interface refraction, slow light, and vortex-like circulation of light, can only be captured through numerical solutions of Maxwell's equations. These unique wave effects are crucial to breaking the Lambertian limit.

The convergence of numerical solutions is vital to accurately predict the absorption in PhC solar cells. The smaller wavelengths are absorbed easily in $c-Si$ due to the relatively high imaginary part of its refractive index. However, due to the weak absorption of $c-Si$ at longer wavelengths, these infrared wavelengths constitute most of the unabsorbed reflected energy. A small part of this unabsorbed energy may be spuriously reflected by the PML, causing residual numerical noise. Consequently, longer wavelength sunlight absorption is more susceptible to spurious numerical noise. This noise appears if the simulation is run for excessively long durations (see Appendix B).

We optimize the $SiO_2-SiN_x-Al_2O_3$ ARC of a $10\mu m$ -thick cell in the $300 - 1100nm$ wavelength range using 140 EMTL steps. As explained in Appendix B, each EMTL step consists of a large number of FDTD iterations. In order to obtain the MAPD over the full wavelength range of $300 - 1200nm$, we augment the $300 - 1100nm$ MAPD of the optimized ARC layer with

the 1100 – 1200nm MAPD computed using 525 EMTL steps. For ARC optimization in the 300 – 1100nm wavelength range, first we keep h_3 fixed at 20nm and optimize h_1 and h_2 . The optimization map in Fig. 2 shows that a maximum MAPD of 40.86mA/cm² over the 300 – 1100nm wavelength range is achieved for $h_1 = 80$ nm and $h_2 = 30$ nm. Next, we set $h_1 = 80$ nm and search for the local maxima in the (h_2, h_3) parameter space, as shown in Fig. 3. The optimization map of Fig. 3(a) shows that the point $h_2 = 30$ nm and $h_3 = 20$ nm is indeed a local maxima with $J_{MAPD} = 40.86$ mA/cm². However, as shown in Fig. 3(b) this MAPD is surpassed by another local maxima at $h_2 = 120$ nm, $h_3 = 150$ nm with $J_{MAPD} = 41.14$ mA/cm². While the MAPD for 80 – 30 – 20 ARC falls slightly below than that of 80 – 120 – 150 ARC, the choice of the former ARC is very close to the choice of $h_1 = 80$ nm, $h_2 = 40$ nm and $h_3 = 20$ nm in much thicker experimentally fabricated POLO cells [7,8]. In order to ascertain that $h_1 = 80$ nm is indeed a local maxima for $h_2 = 120$ nm, $h_3 = 150$ nm, we calculate the MAPD variation versus h_1 (shown in Fig. 4) while keeping h_2 and h_3 fixed at 120nm and 150nm, respectively.

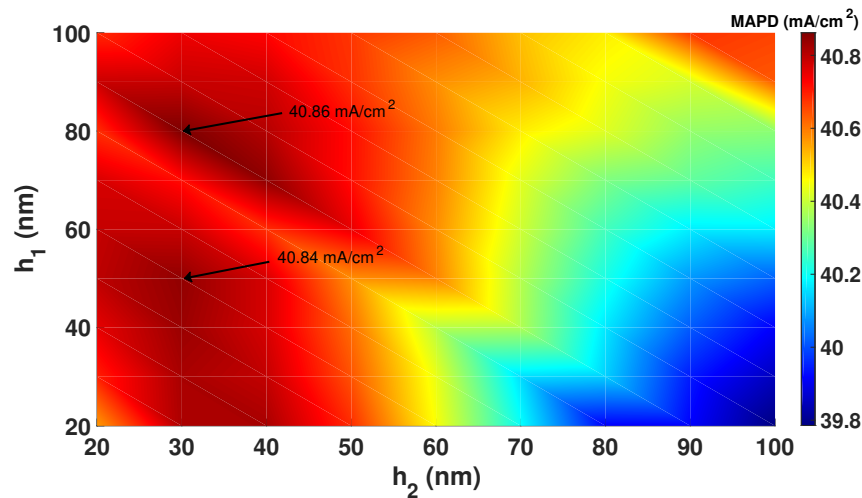


Fig. 2. SiO_2 - SiN_x - Al_2O_3 ARC optimization for the 10 μ m-thick cells with lattice constant $a = 3.1\mu$ m, keeping h_3 fixed at 20nm. The simulations do not include the SiO_2 buffer layer between the silicon and PEC. The map corresponds to only the 300 – 1100nm wavelength range. The optimum MAPD of 40.86mA/cm², for this specific wavelength range, is obtained for $h_1 = 80$ nm and $h_2 = 30$ nm.

Figure 5 shows the 300 – 1200nm absorption spectra of our 10 μ m-thick PhC cell with 80 – 120 – 150 and 80 – 40 – 20 ARCs. Here, the 1100 – 1200nm absorptions are calculated using 520 EMTL steps. Table 1 summarizes the partial MAPDs over different wavelength ranges along with the convergence criteria for both types of ARCs. The total MAPDs over the entire spectral range of 300 – 1200nm are 42.72 and 43.05mA/cm² corresponding to 80 – 40 – 20 and 80 – 120 – 150 ARCs, respectively.

In earlier work [17], we considered a two-layer ARC that consists of hypothetical dielectrics with refractive indices 2.6 adjacent to c – Si and 1.4 at the top, for inverted pyramid, photonic crystals with no mesa between the pyramids ($b = 0$). While this choice is very attractive from the optical performance viewpoint, an additional thin Al_2O_3 layer adjacent to c – Si provides excellent surface passivation [7,8]. In actual fabricated structures [43,45–47] a small mesa, $b \simeq 30$ nm, between pyramids is very likely to occur. In this article, we consider the optimization of the SiO_2 - SiC - Al_2O_3 ARC in our 15 μ m-thick PhC cell. We note that the MAPD in the 300 – 1030nm range converges for 200 EMTL steps (shown in Fig. 15 of Appendix B). Accordingly, we

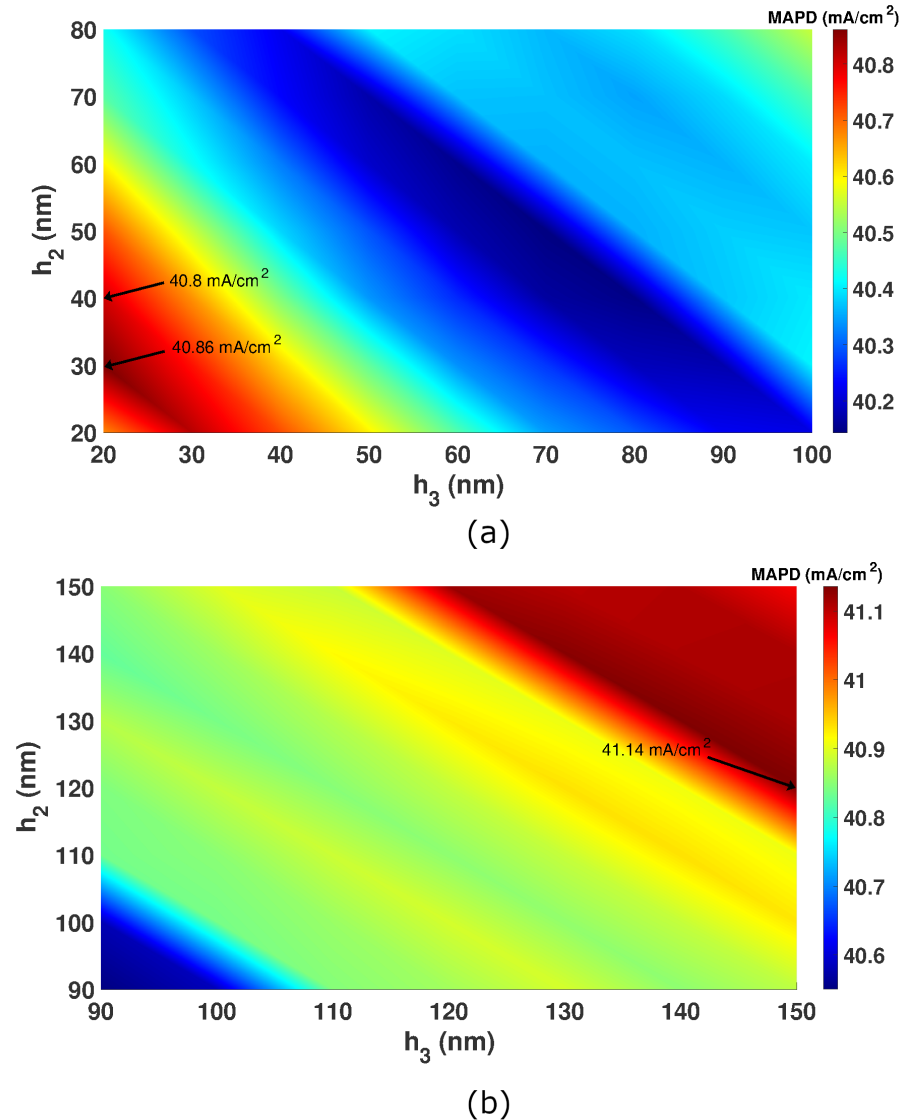


Fig. 3. SiO_2 - SiN_x - Al_2O_3 ARC optimization for $H = 10\mu m$ and $a = 3.1\mu m$: h_1 is kept fixed at $80nm$. The simulations do not include the SiO_2 buffer layer between the silicon and PEC. The MAPD corresponds to only the $300 - 1100nm$ wavelength range. Two local maxima are found (a) $40.86mA/cm^2$ for the $80 - 30 - 20$ ARC and (b) $41.14mA/cm^2$ for the $80 - 120 - 150$ ARC.

choose 200 as the default number of EMTL time-steps in all computations in the $300 - 1030nm$ wavelength range involving the $15\mu m$ -thick PhC cell.

For ARC optimization in the $15\mu m$ -thick PhC cell, we fix the thickness of the Al_2O_3 layer, h_3 , to $10nm$ and vary the thicknesses of the SiO_2 and SiC layers, h_1 and h_2 , simultaneously. Figure 6 shows that a maximum $300 - 1030nm$ MAPD of $39.07mA/cm^2$ is achieved for $h_1 = 90nm$ and $h_2 = 30nm$. Next, we fix h_1 and h_2 to 90 and $30nm$, respectively, and study the effect of h_3 on the optical performance of the cell. Figure 7 shows that a thicker Al_2O_3 passivation layer is detrimental to the optical performance of the cell. As the Al_2O_3 thickness increases from $10nm$

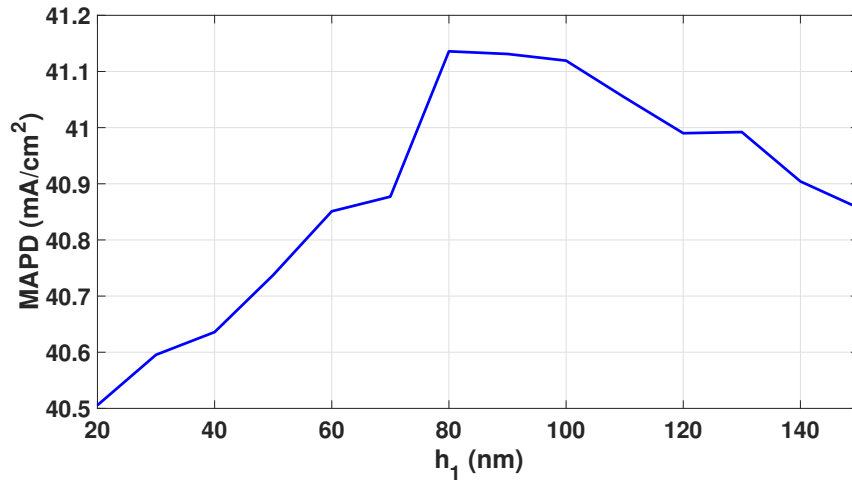


Fig. 4. Variation of 300 – 1100nm MAPD for $H = 10\mu\text{m}$ with h_1 for $h_2 = 120\text{nm}$, $h_3 = 150\text{nm}$ corresponding to $\text{SiO}_2\text{-SiN}_x\text{-Al}_2\text{O}_3$ ARC. This exhibits a local maximum for $h_1 = 80\text{nm}$. The simulations do not include the SiO_2 buffer layer between the silicon and PEC.

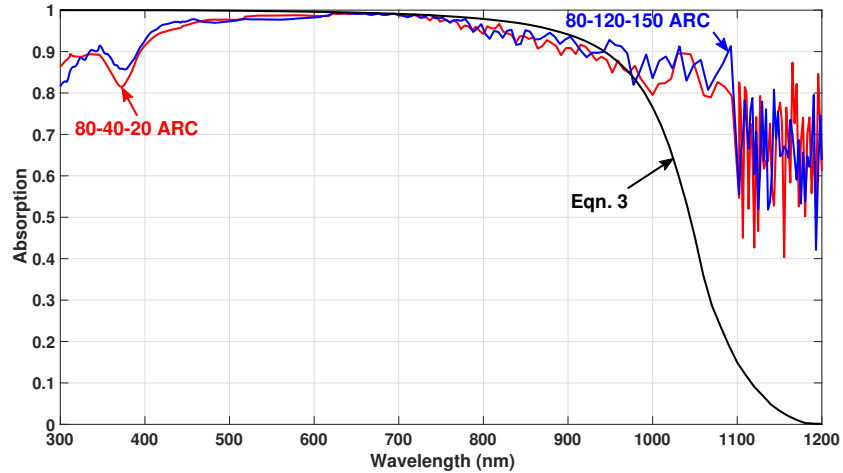


Fig. 5. Absorption spectra in a $10\mu\text{m}$ -thick $c\text{-Si}$ PhC cell, with lattice constant $a = 3.1\mu\text{m}$, mesa $b = 30\text{nm}$, for two different choices of $\text{SiO}_2\text{-SiN}_x\text{-Al}_2\text{O}_3$ ARC. The simulations do not include the SiO_2 buffer layer between the silicon and PEC. The black curve corresponds to the $4n^2$ limit calculated using Eq. (3).

Table 1. Summary of MAPD and convergence for different choices of $\text{SiO}_2\text{-SiN}_x\text{-Al}_2\text{O}_3$ ARCs in $10\mu\text{m}$ -thick inverted pyramid PhC cell with lattice constant $a = 3.1\mu\text{m}$ and mesa $b = 30\text{nm}$. The simulations do not include the SiO_2 buffer layer between the silicon and PEC.

Thickness (μm)	80 – 40 – 20nm anti-reflection coating			80 – 120 – 150nm anti-reflection coating			EMTL time-steps needed to achieve convergence	
	300 – 1100 nm range MAPD (mA/cm^2)	1100 – 1200nm range MAPD (mA/cm^2)	Total (mA/cm^2)	300 – 1100 nm range MAPD (mA/cm^2)	1100 – 1200nm range MAPD (mA/cm^2)	Total (mA/cm^2)	300 – 1100nm MAPD	1100 – 1200nm MAPD
10	40.76	1.96	42.72	41.14	1.91	43.05	140	520

to 30nm , the MAPD decreases by approximately $0.5\text{mA}/\text{cm}^2$. For an increase in thickness from 30nm to 50nm , the approximate loss in MAPD is $0.9\text{mA}/\text{cm}^2$. Our analysis suggests that the thinnest possible Al_2O_3 layer that still yields a sufficient surface passivation is the ideal choice for light-trapping.

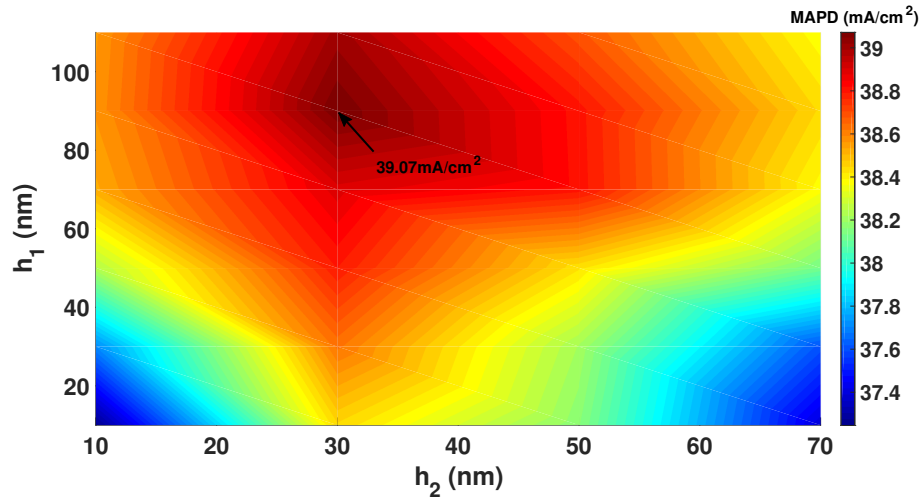


Fig. 6. $\text{SiO}_2\text{-SiC-Al}_2\text{O}_3$ ARC optimization for $H = 15\mu\text{m}$ inverted pyramid PhC cell with lattice constant $a = 3.1\mu\text{m}$ and mesa $b = 30\text{nm}$, keeping h_3 fixed at 10nm . The simulations do not include the SiO_2 buffer layer between the silicon and PEC. The map corresponds to the MAPD over $300 - 1030\text{nm}$ wavelength range. The local maxima occurs at $h_1 = 90\text{nm}$, $h_2 = 30\text{nm}$.

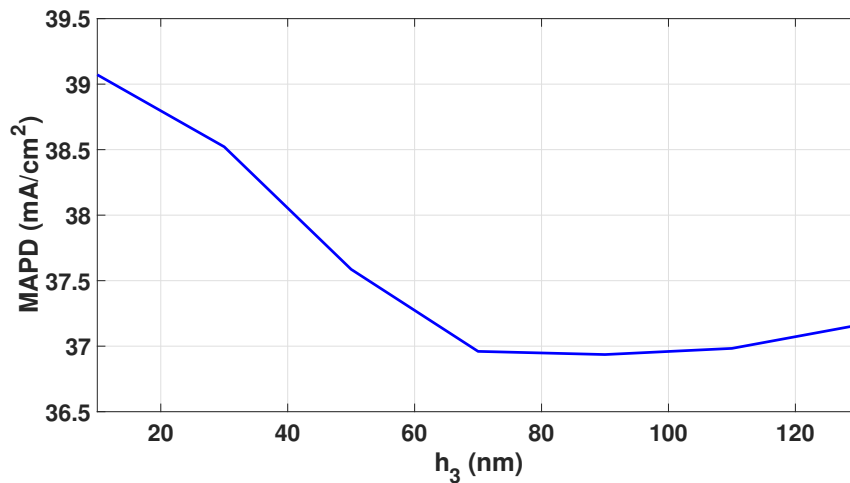


Fig. 7. $300 - 1030\text{nm}$ MAPD variation with Al_2O_3 layer thickness (h_3) for an $H = 15\mu\text{m}$ thick inverted pyramid PhC cell with lattice constant $a = 3.1\mu\text{m}$, mesa $b = 30\text{nm}$ and $\text{SiO}_2\text{-SiC-Al}_2\text{O}_3$ ARC. We keep the thicknesses of the SiO_2 and SiC layers, h_1 and h_2 , fixed at 90nm and 30nm , respectively. The simulations do not include the SiO_2 buffer layer between the silicon and PEC. The thinnest possible layer of Al_2O_3 is ideal for the best optical absorption in Si .

As shown in Fig. 16 of Appendix B, the convergence plateau, corresponding to the long wavelength regime MAPD of our $15\mu\text{m}$ -thick PhC cell with the optimum 90 – 30 – 10 stack of $\text{SiO}_2\text{-SiC-Al}_2\text{O}_3$, appears between 650 to 660 EMTL steps yielding a MAPD of $4.33\text{mA}/\text{cm}^2$. Overall, the $15\mu\text{m}$ -thick inverted pyramid PhC cell with an optimum $\text{SiO}_2\text{-SiC-Al}_2\text{O}_3$ ARC and 30nm mesa leads to an MAPD of $43.4\text{mA}/\text{cm}^2$ over the $300 - 1200\text{nm}$ spectral range. The corresponding $300 - 1200\text{nm}$ range absorption spectrum is shown by the red curve in Fig. 8. Further, we compare the performance of the 80 – 40 – 20 ARC of $\text{SiO}_2\text{-SiN}_x\text{-Al}_2\text{O}_3$ (absorption spectrum shown in blue curve in Fig. 8) with the optimum $\text{SiO}_2\text{-SiC-Al}_2\text{O}_3$ ARC. The $\text{SiO}_2\text{-SiN}_x\text{-Al}_2\text{O}_3$ yields MAPD values of $38.54\text{mA}/\text{cm}^2$ and $4.35\text{mA}/\text{cm}^2$ over the $300 - 1030\text{nm}$ and $1030 - 1200\text{nm}$ wavelength range, respectively. This leads to a total MAPD of $42.89\text{mA}/\text{cm}^2$ over the $300 - 1200\text{nm}$ wavelength range. Clearly, an optimum $\text{SiO}_2\text{-SiC-Al}_2\text{O}_3$ ARC offers $0.51\text{mA}/\text{cm}^2$ more MAPD than the 80 – 40 – 20 ARC of $\text{SiO}_2\text{-SiN}_x\text{-Al}_2\text{O}_3$ for $H = 15\mu\text{m}$.

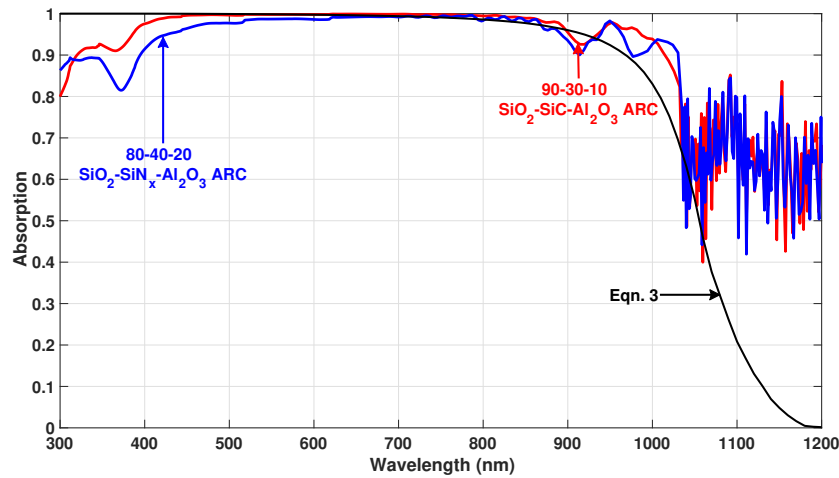


Fig. 8. Absorption spectra in $H = 15\mu\text{m}$ inverted pyramid PhC cell with lattice constant $a = 3.1\mu\text{m}$ and mesa $b = 30\text{nm}$ for two different ARC configurations. The simulations do not include the SiO_2 buffer layer between the silicon and PEC. 90 – 30 – 10 ARC ($\text{SiO}_2\text{-SiC-Al}_2\text{O}_3$): MAPDs over $300 - 1030\text{nm}$ and $1030 - 1200\text{nm}$ wavelength ranges are $39.07\text{mA}/\text{cm}^2$ and $4.33\text{mA}/\text{cm}^2$, respectively (total $43.4\text{mA}/\text{cm}^2$). 80 – 40 – 20 ARC ($\text{SiO}_2\text{-SiN}_x\text{-Al}_2\text{O}_3$): MAPDs over $300 - 1030\text{nm}$ and $1030 - 1200\text{nm}$ wavelength ranges are $38.54\text{mA}/\text{cm}^2$ and $4.35\text{mA}/\text{cm}^2$, respectively (total $42.89\text{mA}/\text{cm}^2$). The black curve corresponds to the $4n^2$ limit calculated using Eq. (3).

The MAPD of $43.4\text{mA}/\text{cm}^2$ in a $15\mu\text{m}$ -thick cell with the optimum $\text{SiO}_2\text{-SiC-Al}_2\text{O}_3$ is smaller than the MAPD of $44.39\text{mA}/\text{cm}^2$ for a $15\mu\text{m}$ -cell with a two-layer ARC described in previous studies [17]. Our analysis shows that much of this improved MAPD results from adding a 50nmSiO_2 buffer layer [17] between the $c - \text{Si}$ and the metal back-reflector of the cell. The comparison of absorptions with and without the buffer layer in Fig. 9 shows that the addition of the SiO_2 buffer improves the overall absorption in the $15\mu\text{m}$ cell for wavelengths beyond 900nm , yielding a total MAPD of $44.03\text{mA}/\text{cm}^2$ over the $300 - 1200\text{nm}$ wavelength range. The difference of $0.36\text{mA}/\text{cm}^2$ MAPD between this study and earlier work [17] can be attributed to the addition of a 30nm mesa between pyramids (present case), the use of refractive index 1.47 for the top ARC layer, and a different breakup of the $300 - 1200\text{nm}$ into two segments in determining FDTD convergence plateaus. This difference in MAPD leads to a $\sim 0.3\%$ additive change in the power conversion efficiency (see Table 3 in [18]). Our present FDTD analysis, with explicit convergence criteria, reinforces the major conclusion that $15\mu\text{m}$ -thick PhC solar cell may achieve beyond 30% power conversion efficiency, as suggested earlier [17].

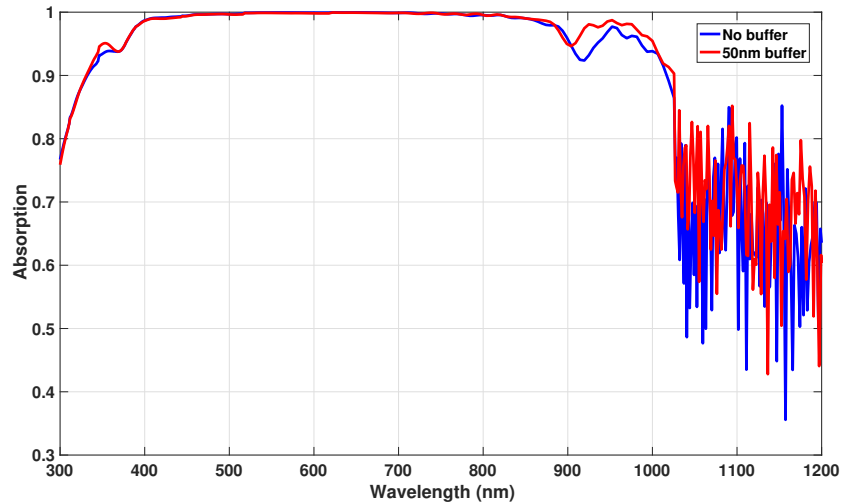


Fig. 9. Absorption spectra in $H = 15\mu\text{m}$ inverted pyramid PhC cell with lattice constant $a = 3.1\mu\text{m}$ and mesa $b = 30\text{nm}$, and a dual layer 100 – 45 ARC of $\text{SiO}_2 - \text{SiC}$. Red curve: absorption with a 50nmSiO_2 buffer layer between $c - \text{Si}$ and the metal back-reflector. The partial MAPDs of $39.3\text{mA}/\text{cm}^2$ and $4.73\text{mA}/\text{cm}^2$ over the 300 – 1030nm and 1030 – 1200nm wavelength ranges yield a total MAPD of $44.03\text{mA}/\text{cm}^2$. Blue curve: absorption in absence of a SiO_2 buffer layer. This corresponds to $39.16\text{mA}/\text{cm}^2$ and $4.37\text{mA}/\text{cm}^2$ partial MAPDs over the 300 – 1030nm and 1030 – 1200nm wavelength ranges, respectively, leading to a total MAPD of $43.5\text{mA}/\text{cm}^2$.

The existence of the SiO_2 buffer layer at the back surface of an actual solar cell is essential in order to passivate the back surface. In addition to providing better passivation, the buffer layer also compensates for the real world effects such as reduced reflection and parasitic absorption introduced by the use of actual metals instead of PEC. Both numerical simulations [42] and experimental data [52] suggest that the combination of a SiO_2 buffer and Ag back-reflector provide practically the same performance as the SiO_2 -PEC combination.

4. Wave-interference-based light trapping in thick silicon

In order to obtain convergence over the 300 – 1200nm wavelength range for $H \geq 50\mu\text{m}$, we divide the entire wavelength range into three parts: 300 – 550nm with 20nm spatial resolution, 550 – 900nm and 900 – 1200nm with 30nm spatial resolution. We perform separate computations over each of the wavelength ranges. As shown in the Fig. 17 of Appendix B, the 900 – 1200nm range MAPD of the $50\mu\text{m}$ -thick PhC cell with 80 – 40 – 20 SiO_2 - SiN_x - Al_2O_3 ARC converges after 600 EMTL steps yielding a MAPD of $10.30\text{mA}/\text{cm}^2$. We plot the 300 – 1200nm absorption spectra in the 50 and $100\mu\text{m}$ -thick cells for different choices of ARCs in Fig. 10(a) and (b), respectively. The red and blue curves correspond to the absorptions in the PhC cells with 80 – 40 – 20 and 80 – 120 – 150 ARCs of SiO_2 - SiN_x - Al_2O_3 , respectively. The closely spaced, sharp resonances in the long-wavelength region of the absorption spectra correspond to different slow-light modes in the PhC (see Fig. 18 in Appendix B). Table 2 summarizes the partial MAPDs for different wavelength ranges and the overall MAPDs in 50 and $100\mu\text{m}$ -thick PhC cells with different ARC layers. Unlike the $15\mu\text{m}$ -thick cell, replacing the SiN_x layer with SiC doesn't lead to a significant improvement in the solar absorption for $H \geq 50\mu\text{m}$. The 80 – 40 – 20 ARC of SiO_2 - SiN_x - Al_2O_3 offers slightly better performance than the 80 – 120 – 150 counterpart in the 300 – 900nm wavelength range for both 50 and $100\mu\text{m}$ -thick cells. However, in the $50\mu\text{m}$ PhC cell the 80 – 120 – 150 ARC performs better in the 900 – 1200nm wavelength range,

leading to $0.31\text{mA}/\text{cm}^2$ MAPD improvement over the $300 - 1200\text{nm}$ range compared to the $80 - 40 - 20$ ARC. The $50\mu\text{m}$ -thick cell is capable of achieving overall MAPD values of 43.22 , 43.22 and $43.53\text{mA}/\text{cm}^2$ with $80 - 40 - 20\text{SiO}_2\text{-SiN}_x\text{-Al}_2\text{O}_3$, $80 - 40 - 20\text{SiO}_2\text{-SiC-Al}_2\text{O}_3$ and $80 - 120 - 150\text{SiO}_2\text{-SiN}_x\text{-Al}_2\text{O}_3$ ARCs, respectively. In contrast, for the $100\mu\text{m}$ -thick cell the choice of $80 - 120 - 150$ ARC offers almost similar performance as the $80 - 40 - 20$ ARC. By doubling the cell thickness to $100\mu\text{m}$, the MAPDs are improved by only $0.68\text{mA}/\text{cm}^2$ and $0.34\text{mA}/\text{cm}^2$ for the $80 - 40 - 20$ and $80 - 120 - 150$ ARCs, respectively.

Table 2. Summary of the optical performance of 50 and $100\mu\text{m}$ -thick PhC cell with different choices of 3-layer ARC. The last two columns show the number of EMTL steps used in the computations. All cells have inverted pyramid lattice constants of $a = 3.1\mu\text{m}$ and mesas between pyramids of 30nm . The simulations do not include the SiO_2 buffer layer between the silicon and PEC.

Thickness (μm)	80 – 40 – 20SiO ₂ -SiN _x -Al ₂ O ₃ ARC			80 – 40 – 20SiO ₂ -SiC-Al ₂ O ₃ ARC			80 – 120 – 150SiO ₂ -SiN _x -Al ₂ O ₃ ARC			EMTL time-steps for convergence	
	300 – 900 nm range MAPD (mA/cm^2)	900 – 1200nm range MAPD (mA/cm^2)	Total (mA/cm^2)	300 – 900 nm range MAPD (mA/cm^2)	900 – 1200nm range MAPD (mA/cm^2)	Total (mA/cm^2)	300 – 900 nm range MAPD (mA/cm^2)	900 – 1200nm range MAPD (mA/cm^2)	Total (mA/cm^2)	300 – 900nm MAPD	900 – 1200nm MAPD
50	32.92	10.30	43.22	32.94	10.28	43.22	32.77	10.76	43.53	160	640
100	32.93	10.97	43.9	32.94	10.97	43.91	32.77	11.1	43.87	200	1200

Traditional $c - \text{Si}$ solar cells are typically more than $150\mu\text{m}$ thick. When the front surfaces are textured with feature sizes much larger than the wavelength of light, ray-tracing may be applied to model the light-trapping. In contrast, the feature sizes in our PhC cells are comparable to the wavelength of light and numerical solution of Maxwell's equations is essential to accurately describe the light-trapping in such cells. Accurate prediction of solar absorption in thick PhC cells involving wave-interference effects, requires very long computation time and high memory usage. While thin $10 - 20\mu\text{m}$ PhC cells provide the most attractive route towards very high conversion efficiency, a comparison with thicker $100 - 300\mu\text{m}$ cells is instructive. Moreover, PhC can be readily incorporated in thicker $c - \text{Si}$ cells with well-established fabrication process flow [45].

In Fig. 11, we show the $300 - 1200\text{nm}$ wavelength range absorption spectra, computed using FDTD, for 150 , 190 and $300\mu\text{m}$ -thick PhC cells with $80 - 40 - 20$ (red curve) and $80 - 120 - 150$ ARCs (blue curve) of $\text{SiO}_2\text{-SiN}_x\text{-Al}_2\text{O}_3$. The black curve shows the reference absorption spectrum of the $4n^2$ limit, calculated using the following equation [18,19]:

$$A_T = \frac{\alpha_{\text{Si}} 4n^2 H}{1 + \alpha_{\text{Si}} 4n^2 H} \quad (3)$$

Here, the wavelength dependent absorption coefficient of $c - \text{Si}$, α_{Si} , and the real part of refractive index, n , are taken from Green and Keevers [53]. The summary of the computed MAPDs in Table 3 shows that the $300 - 900\text{nm}$ range MAPD is essentially independent of the cell-thickness in this range and the type of ARC used. A comparison with the Table 2 reveals that the $300 - 900\text{nm}$ MAPD remains approximately the same for $H \geq 50\mu\text{m}$ for either ARC configurations. Figure 11 shows that for $H \geq 150\mu\text{m}$ the performance of $80 - 120 - 150$ ARC deteriorates beyond 800nm in comparison to the $80 - 40 - 20$ ARC. The $80 - 120 - 150$ ARC yields approximately $0.7\text{mA}/\text{cm}^2$ less MAPD in comparison to the $80 - 40 - 20$ ARC over the entire wavelength of $300 - 1200\text{nm}$. For the $150\mu\text{m}$ -thick cell, the overall MAPDs corresponding to the $80 - 40 - 20$ and $80 - 120 - 150$ ARCs are 45.22 and $44.51\text{mA}/\text{cm}^2$, respectively. There is practically no improvement in MAPD as the cell-thickness is increased beyond $150\mu\text{m}$. However, increased thickness would lead to increased Auger recombination of the photo-generated charge carriers. Accordingly, the photovoltaic conversion efficiency of the PhC cells with $150 < H < 300\mu\text{m}$ would be worse than the $150\mu\text{m}$ -thick PhC cell.

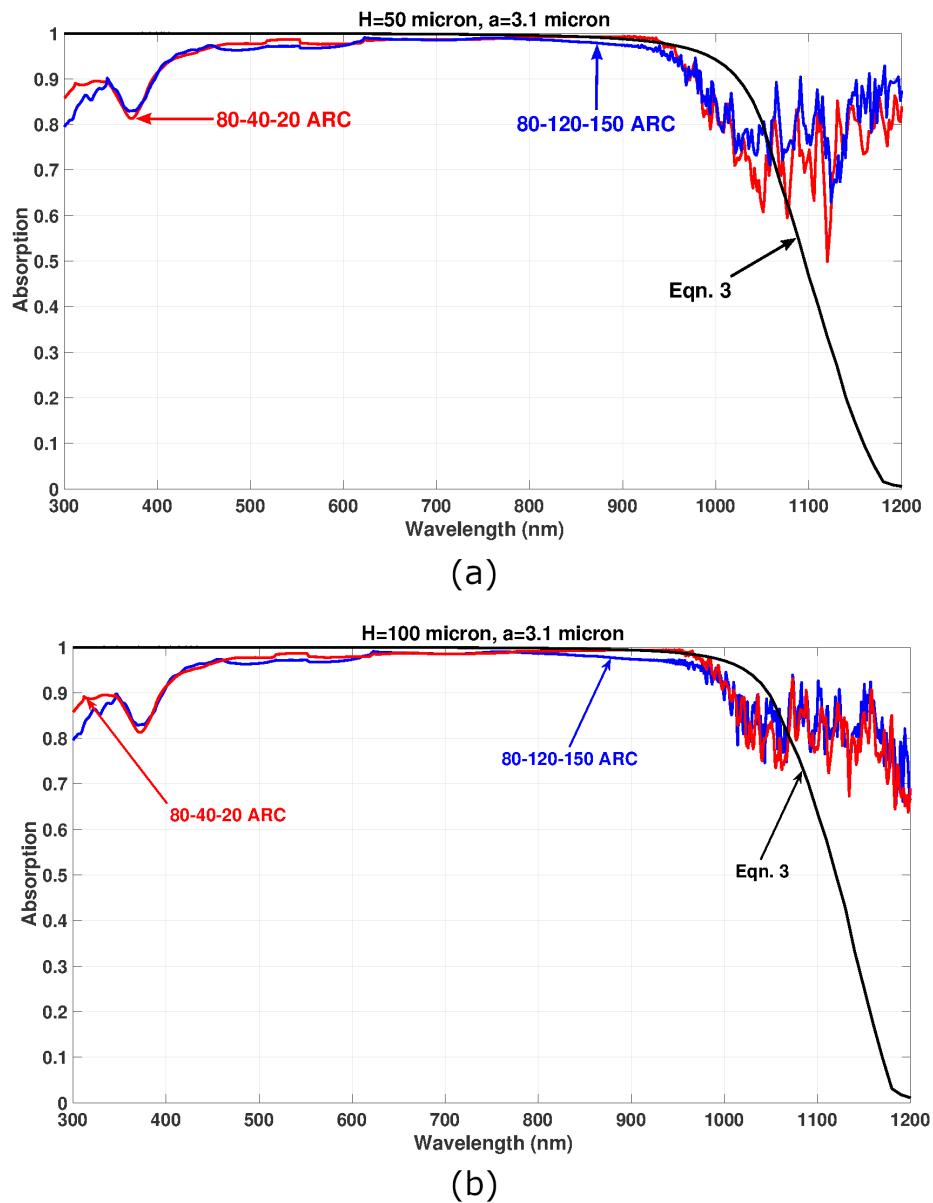


Fig. 10. 300 – 1200nm absorption for PhC cells with different choices of SiO_2 - SiN_x - Al_2O_3 ARCs. (a) $H = 50\mu m$: the 80 – 120 – 150 ARC performs slightly better with a MAPD of $43.53mA/cm^2$ in comparison to the $43.22mA/cm^2$ of the 80 – 40 – 20 ARC. (b) $H = 100\mu m$: Both ARCs offer similar performance with $43.87mA/cm^2$ using 80 – 120 – 150 ARC and $43.9mA/cm^2$ using 80 – 40 – 20 ARC. In all cases, the lattice constant is chosen as $a = 3.1\mu m$ and a mesa of $b = 30nm$ between pyramids is included. The simulations do not include the SiO_2 buffer layer between the silicon and PEC. The black curve corresponds to the $4n^2$ limit calculated using Eq. (3).

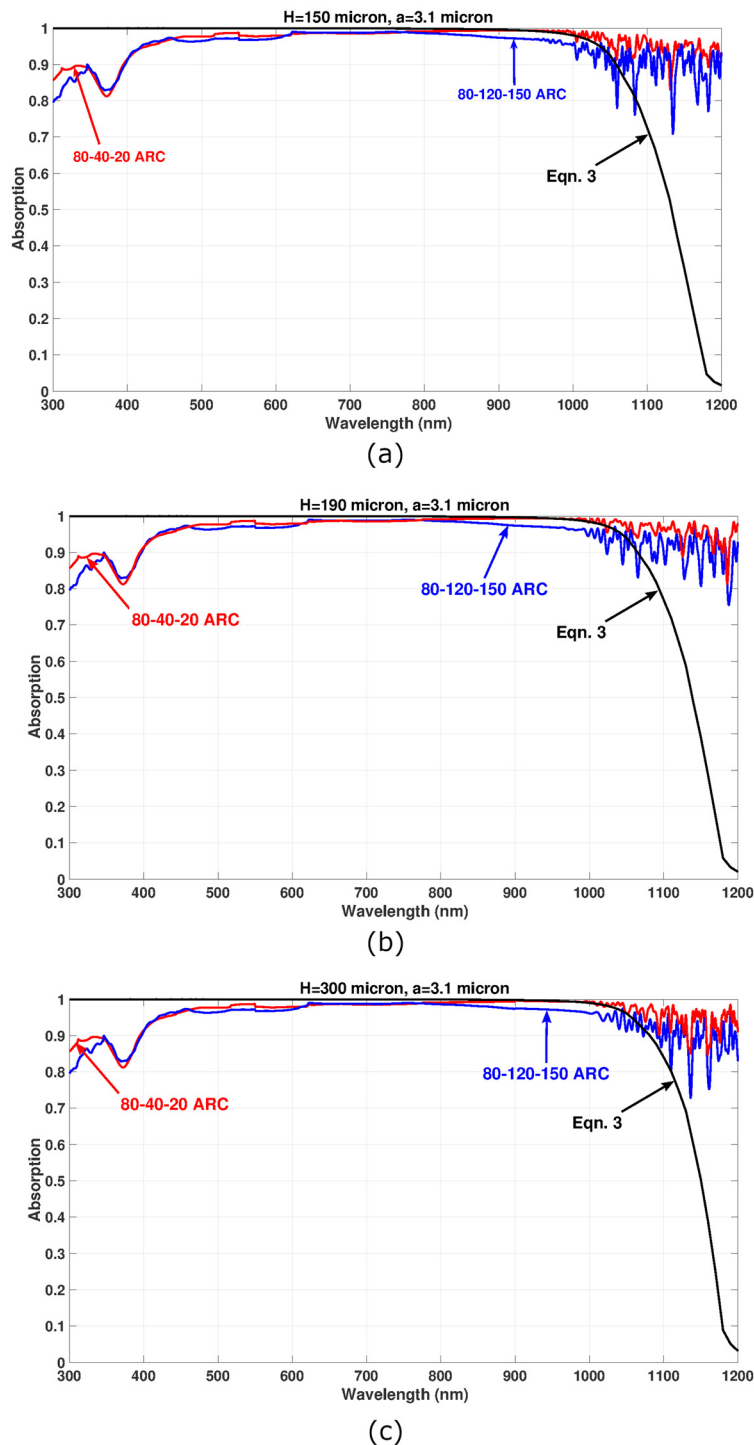


Fig. 11. 300 – 1200nm absorption spectra in thick *c* – Si PhC solar cells, with lattice constant $a = 3.1\mu\text{m}$ and mesa $b = 30\text{nm}$, for different choices of $\text{SiO}_2\text{-SiN}_x\text{-Al}_2\text{O}_3$ ARC. (a) $H = 150\mu\text{m}$, (b) $H = 190\mu\text{m}$ and (c) $H = 300\mu\text{m}$. The black curve corresponds to the $4n^2$ limit calculated using Eq. (3). Unlike the $50\mu\text{m}$ -thick PhC cell, 80 – 40 – 20 ARC performs better than the 80 – 120 – 150 ARC. The simulations do not include the SiO_2 buffer layer between the silicon and PEC.

Table 3. MAPD summary for 150 – 300 μm -thick cells. All cells have inverted pyramid textures on their top surfaces with lattice constant $a = 3.1\mu\text{m}$ and mesa $b = 30\text{nm}$ between pyramids. The simulations do not include the SiO_2 buffer layer between the silicon and PEC.

Thickness (μm)	80 – 40 – 20 SiO_2 - SiN_x - Al_2O_3 ARC			80 – 120 – 150 nmSiO_2 - SiN_x - Al_2O_3 ARC			EMTL time-steps needed to achieve convergence	
	300 – 900 nm range MAPD (mA/cm^2)	900 – 1200nm range MAPD (mA/cm^2)	Total (mA/cm^2)	300 – 900 nm range MAPD (mA/cm^2)	900 – 1200nm range MAPD (mA/cm^2)	Total (mA/cm^2)	300 – 900nm MAPD	900 – 1200nm MAPD
150	32.93	12.29	45.22	32.77	11.74	44.51	280	1460
190	32.93	12.35	45.28	32.77	11.84	44.61	300	1720
300	32.93	12.35	45.28	32.77	11.88	44.65	380	2750

5. Conclusion

In summary, our well-converged FDTD simulations of 50 – 300 μm -thick inverted pyramid PhC solar cells provide a roadmap to high efficiency c – Si solar cells using fabricated photonic crystals with 3.1 μm lattice constant [45–47]. However, the sunlight absorption may be improved through further optimization of lattice constants and better choices of ARC in 16 – 100 μm -thick PhC cells. Table 1 in [17] shows that better choices of lattice constants exist for 18 μm and 20 μm -thick PhC cells than our current choice of $a = 3.1\mu\text{m}$. Nevertheless, our results, based on 3.1 μm lattice constant, provide valuable lower bounds on attainable MAPD for cells of various thickness. They reveal that exploiting the wave nature of light offers an important avenue for improving the short circuit current of state-of-the-art silicon solar cells.

While previous high efficiency c – Si cells provide state-of-the-art electronic performance, the photo-current densities still fall well below the statistical ray-trapping limits. Figure 12 shows that the recent c – Si cells (with more than 26% power conversion efficiency) have photo-current densities significantly below the $4n^2$ limit. The photo-current densities of the Kaneka, POLO-IBC and Longi cells range between 41.4 – 42.65 mA/cm^2 . In contrast, the wave-interference-based (beyond ray-optics limit) light trapping in our inverted pyramid PhCs offers MAPD of 45.22 mA/cm^2 for a 150 μm -thick cell. This is feasible with well-established ARC and passivation. The 130 μm -thick Longi cell offers a better V_{OC} at the expense of a significantly reduced photo-current density of 41.45 mA/cm^2 that falls well below the $4n^2$ limit. In contrast, Fig. 12 show that the PhC cells, with 3.1 μm lattice constant, maintain MAPDs beyond the $4n^2$ limit for the entire 10 – 300 μm range of c – Si thickness. Such sunlight trapping and absorption may be vital to achieve c – Si cells with efficiencies beyond 27.1%. The inverted pyramid PhCs can be readily etched on the top surface of the future cells to boost the power conversion efficiency significantly. Further, a significant improvement in conversion efficiency may be achieved by reducing the thickness of the PhC cells below 100 μm . While a reduction in thickness provides increased open-circuit voltage, the thinner inverted pyramid PhC cells maintain more than 43 mA/cm^2 MAPD due to wave-interference-based light-trapping. Electron-hole pair generation profile, obtained from the light-trapping in silicon PhC illustrated in this article, coupled with further numerical solution of the semiconductor drift-diffusion equations and optimization of the doping profiles and contact geometries would provide an accurate estimate of the conversion efficiencies of intermediate-thickness PhC cells [17,20,54]. We hope that our analysis provides a useful roadmap for systematic reduction in silicon solar cell thickness, while at the same time achieving higher power conversion efficiency.

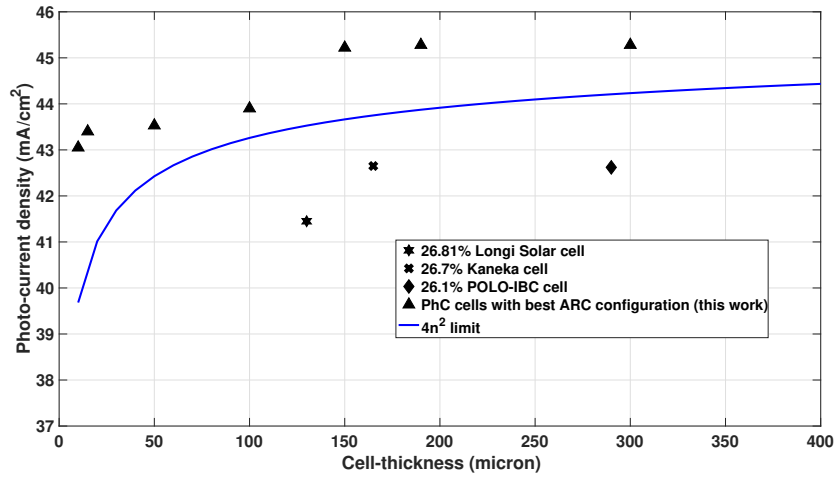


Fig. 12. Comparison of numerically simulated photonic crystal cells (black triangles) with existing cells and $4n^2$ limit. All PhC cell simulations involve inverted pyramid arrays with lattice constant $a = 3.1\mu\text{m}$ and mesa $b = 30\text{nm}$ between pyramids. The simulations of photonic crystal cells do not include the SiO_2 buffer layer between the silicon and PEC.

Appendix A: $c - \text{Si}$ dispersion in the 1000 – 1200nm wavelength range

The dispersion relation of $c - \text{Si}$ in the 1000 – 1200nm wavelength range is modeled by fitting the experimental data of [55] with the following series:

$$\epsilon(\omega) = \epsilon_\infty + \sum_j \frac{\Delta\epsilon_j \omega_{pj}^2}{(\omega_{pj}^2 - 2i\omega\gamma_j - \omega^2)} \quad (4)$$

Each term in the summation, above, represents a Lorentz oscillator. The fitting parameters ϵ_∞ , ω_{pj} , $\Delta\epsilon_j$ and γ_j are determined using a freely available MATLAB fitting program [56]. The experimental data is fitted to 5 Lorentz oscillator terms. The results of the fitting is shown in Table 4. Here, the fitting parameters are artificially truncated after 6 decimal places. The actual fitting parameters, generated from MATLAB are considerably more precise. It is crucial to import the raw data of the fitting program without any truncation to plotting softwares. The fitting program specifies the true fitting parameters to an accuracy of 10^{-15} and can resolve the imaginary part of the permittivity to values as small as 10^{-12} . Feeding truncated data directly into a plotting program can give rise to negative values of the imaginary part of the refractive indices beyond 1100nm wavelength, giving rise to unstable FDTD simulations.

Table 4. Fitting parameters for Si dispersion in the long-wavelength range. The entries are truncated artificially after 6 decimal places.

Wavelength range	ϵ_∞	$\Delta\epsilon_j$	$\omega_{pj}(\times 10^3 \mu\text{m}^{-1})$	$\gamma_j(\times 10^3 \mu\text{m}^{-1})$
1000 – 1200 nm	1.0	0.971156	0.001805	0.000000
		7.244785	0.006785	0.000001
		0.000580	0.001018	0.000047
		2.519084	0.002291	0.000000
		-0.057262	0.001237	0.000004

The data generated by the fitting program, without any truncation, are as follows: $\epsilon_\infty = 1.000002224030137$, $\Delta\epsilon_1 = 0.971155812653212$, $\omega_{p1} = 0.001804694027197$, $\gamma_1 =$

$2.798140199336552 \times 10^{-07}$, $\Delta\epsilon_2 = 7.244784855570929$, $\omega_{p2} = 0.006784588003446$, $\gamma_2 = 8.967371276438763 \times 10^{-07}$, $\Delta\epsilon_3 = 5.798409641567708 \times 10^{-04}$, $\omega_{p3} = 0.001018321969102$, $\gamma_3 = 4.672080308185805 \times 10^{-05}$, $\Delta\epsilon_4 = 2.519084073948060$, $\omega_{p4} = 0.00229063207323632$, $\gamma_4 = 1.79717352111197 \times 10^{-15}$, $\Delta\epsilon_5 = -0.057261802823575$, $\omega_{p5} = 0.00123686786367826$, $\gamma_5 = 4.05282416336000 \times 10^{-06}$.

Appendix B: convergence of FDTD solutions and slow-light modes

Typically, the convergence is determined from a plateau in the variation of inferred MAPD with FDTD time-steps. During the initial stage of the time-stepping, the reflection flux plane records a small amount of flux, mostly due to the reflection from the ARC and front surface of $c - Si$. In this early stage, $A(\lambda)$ and J_{MAPD} appear temporarily elevated. As the time-stepping progresses, the reflection flux plane detects the unabsorbed energy escaping from the interior of the cell. This leads to a decrease in inferred MAPD. Eventually, untrapped energy escapes the cell completely and the MAPD achieves a steady state plateau. The remaining trapped light persists within the structure until it is eventually absorbed as suggested by independent FEM simulations [57] and experimental observations [43]. A small part of the untrapped, unabsorbed energy, previously detected by the reflection flux plane, is reflected from the PML back to the computation cell. This contributes to the simulation artifact that may be detected again at the reflection plane. Indeed, light that is detected more than once by the flux plane may appear as reflection coefficient $R(\lambda) > 1$ and as a spurious negative absorption at some wavelengths. The temporal width of the incident pulse is sufficiently narrow to cover a broad band of frequencies. When the time stepping is carried out beyond the convergence plateau, $R(\lambda)$ starts increasing due to spurious reflection from PML. This simulation artifact is amplified at long wavelengths by the input pulse amplitude which normalizes $R(\lambda)$. This causes $A(\lambda)$ to decrease as time-stepping progresses beyond the plateau. This is most noticeable at infrared wavelengths. The duration of this plateau is governed by the thickness of the cell. The unabsorbed energy decreases with increasing cell-thickness, implying less spurious reflection by the PML. This leads to a longer convergence plateau for

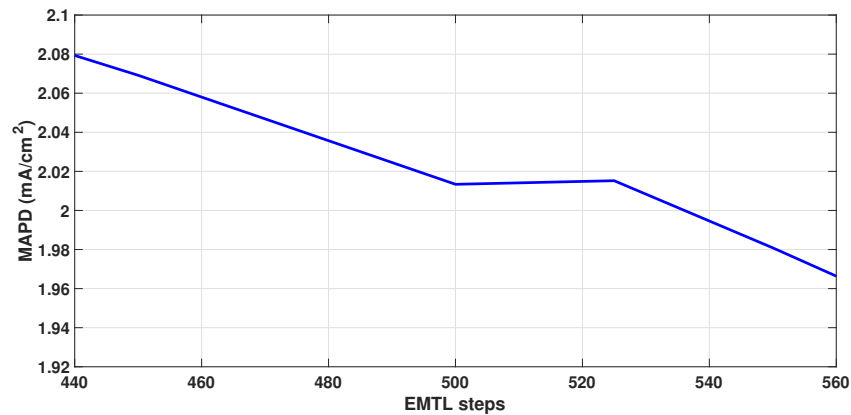


Fig. 13. The inferred MAPD vs. EMTL time steps is calculated from $(1 - R)$ at different EMTL steps, where R is the reflection coefficient measured by a detector plane above the solar cell. A perfect electric conductor (PEC) is placed below the cell to prevent transmission. The simulations do not include the SiO_2 buffer layer between the silicon and PEC. Depicted is 1100 – 1200nm MAPD convergence for $H = 10\mu m$ (without ARC), $a = 3.1\mu m$. The convergence plot exhibits the plateau between 500 – 525 EMTL steps (equivalent to 1443 FDTD iterations). Beyond the convergence plateau, the inferred MAPD continues to decay due to simulation artifact.

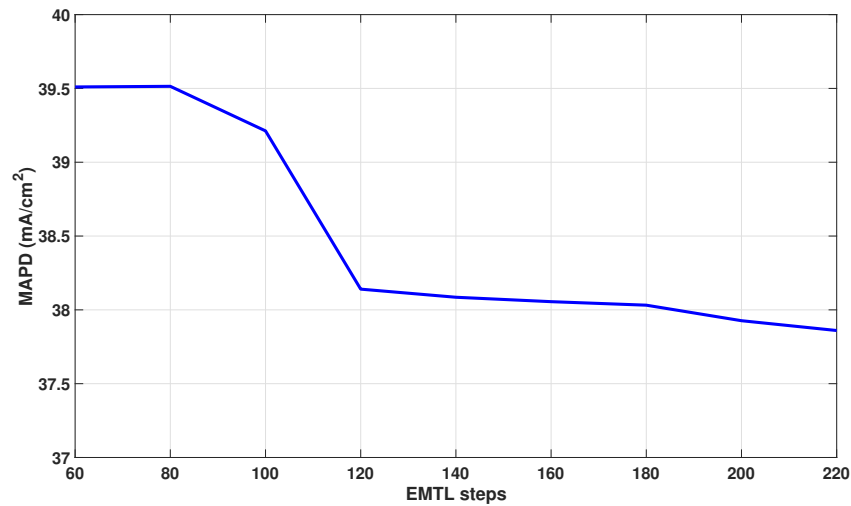


Fig. 14. Inferred MAPD from reflection $R(\lambda)$ over the wavelength range of 300 – 1100nm for $H = 10\mu\text{m}$ (without ARC and SiO_2 buffer) and $a = 3.1\mu\text{m}$ as detected by the flux plane above the solar cell. The plateau over 140 – 180 EMTL steps is more pronounced than in Fig. 13 due to stronger intrinsic absorption and less simulation artifact at smaller wavelengths.

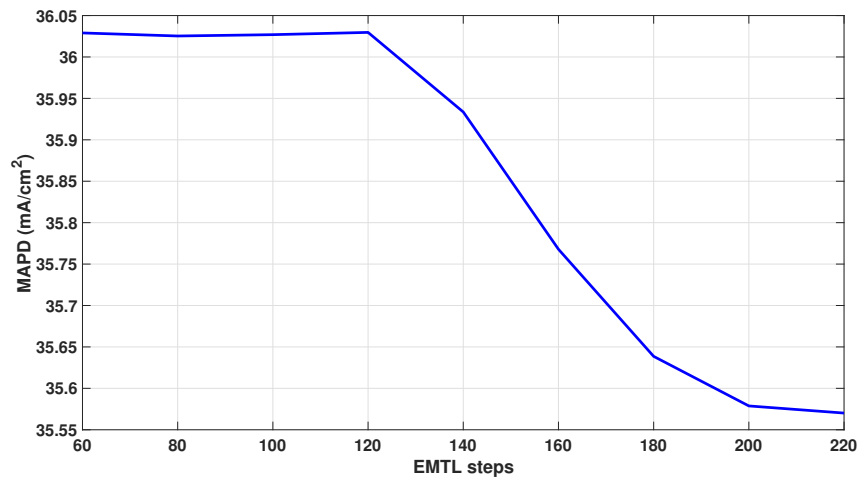


Fig. 15. Convergence plot for 300 – 1030nm MAPD for $H = 15\mu\text{m}$ inverted pyramid PhC cell, with lattice constant $a = 3.1\mu\text{m}$ and mesa $b = 30\text{nm}$, without ARC and SiO_2 buffer. The convergence plateau emerges after 200 EMTL time steps.

thicker cells. Our use of the plateau as a convergence criterion agrees with recent experimental measurements carried out on $10\mu\text{m}$ -thick PhCs [43] as well as with the numerical simulations of $c - \text{Si}$ PhC structures that use finite element methods [27,57].

Figure 13 shows the convergence of 1100 – 1200nm MAPD for $10\mu\text{m}$ -thick inverted pyramid PhC cell without any ARC. The lattice constant of this photonic crystal is $3.1\mu\text{m}$ rather than the optimum $2.5\mu\text{m}$ value determined previously [31]. The convergence plateau appears between 500 and 525 EMTL steps. The number of EMTL time-steps can be converted to the number of FDTD iterations according to the following recipe. First, we calculate Δt using the spatial

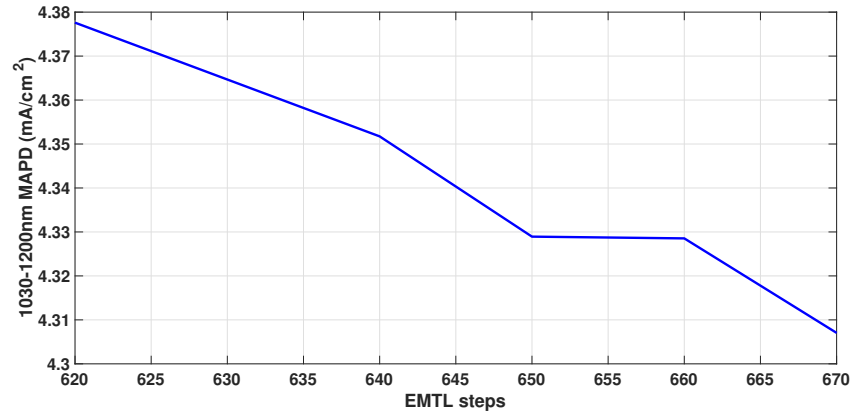


Fig. 16. MAPD convergence for the 1030 – 1200nm wavelength range for an $H = 15\mu\text{m}$ inverted pyramid PhC cell with lattice constant $a = 3.1\mu\text{m}$ and mesa $b = 30\text{nm}$, and 90 – 30 – 10 ARC of $\text{SiO}_2\text{-SiC-Al}_2\text{O}_3$. The simulations do not include the SiO_2 buffer layer between the silicon and PEC. The convergence plateau, appearing at 650 EMTL steps, shows that the MAPD remains stable at $4.33\text{mA}/\text{cm}^2$ over 577 FDTD iterations.

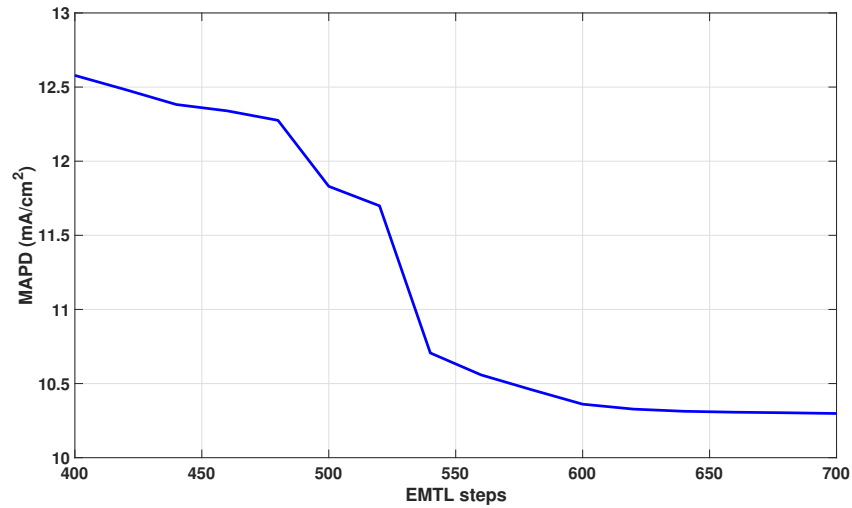


Fig. 17. 900-1200nm MAPD convergence for the $50\mu\text{m}$ -thick inverted pyramid PhC cell with lattice constant $a = 3.1\mu\text{m}$, mesa $b = 30\text{nm}$, and 80 – 40 – 20 ARC of $\text{SiO}_2\text{-SiN}_x\text{-Al}_2\text{O}_3$. The simulations do not include the SiO_2 buffer layer between the silicon and PEC. Since thicker cells absorb more of the longer wavelengths, the convergence plateau suffers from less numerical simulation artifact in comparison to thinner cells.

resolutions Δx , Δy , Δz and the Courant factor S as:

$$\Delta t = \frac{S}{c} \sqrt{(\Delta x)^2 + (\Delta y)^2 + (\Delta z)^2} \quad (5)$$

The speed of light in EMTL is normalized to unity. Further, our simulation assumes $\Delta x = \Delta y = \Delta z = 0.02$ (since, unit of length is set to $1\mu\text{m}$ in our EMTL simulations) and $S = 0.5$. Substituting these values in Eq. (5), we get $\Delta t = 0.01732$ EMTL unit of time. Thus, 25 EMTL steps correspond to $25/\Delta t \approx 1443$ FDTD iterations. A stable MAPD over 1443 iterations implies a steady state FDTD solution. As shown in Fig. 14, 300 – 1100nm MAPD in a $10\mu\text{m}$ -thick

cell converges to a much earlier EMTL plateau (starting near 140 EMTL time-steps) due to the stronger intrinsic absorption and relatively lower simulation artifact from smaller wavelengths.

Figure 15 plots the convergence of the 300 – 1030nm MAPD of the 15 μm -thick PhC cell without any ARC and SiO_2 buffer. The PhC cell has a lattice constant of 3.1 μm and mesa of 30nm. The 300 – 1030nm MAPD converges after 200 EMTL steps.

Figure 16 shows the convergence plot for the long wavelength regime MAPD of our 15 μm -thick PhC cell with the optimum 90 – 30 – 10 stack of SiO_2 - SiC - Al_2O_3 . The plateau appears between 650 to 660 EMTL steps.

Figure 17 plots the 900 – 1200nm range MAPD convergence of the 50 μm -thick PhC cell with 80 – 40 – 20 SiO_2 - SiN_x - Al_2O_3 ARC. The convergence plot exhibits a plateau after 600 EMTL steps with a converged MAPD of 10.30 mA/cm^2 . The duration of the plateau is significantly longer than those in $H = 10$ and 15 μm cells, due to less numerical simulation artifact in the simulations of thicker cells.

Figure 18 shows the distribution of the normalized electric field intensity over the central xz -plane of the 50 μm -thick PhC cell with 80 – 40 – 20 SiO_2 - SiN_x - Al_2O_3 ARC. This plot corresponds to a slow-light resonance at 1087nm, as shown in Fig. 10(a). The magnified view of a portion of the PhC depicts the in-plane Poynting vectors, showing different slow-light modes, such as

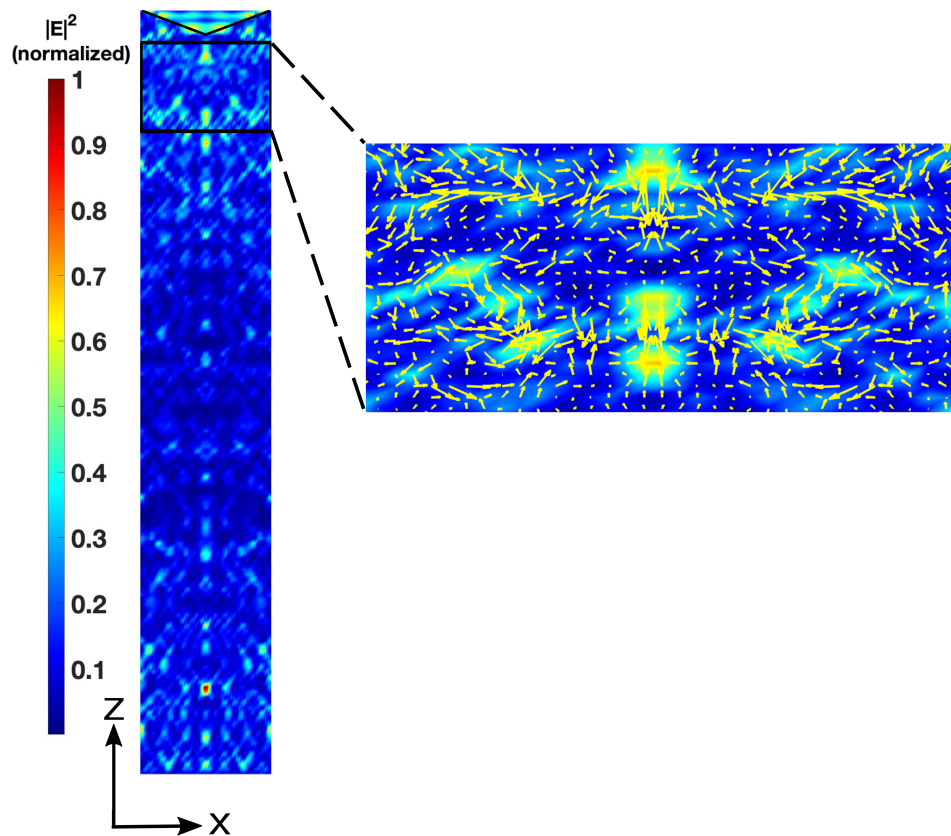


Fig. 18. Distribution of normalized electric field intensity, corresponding to a photonic resonance at 1087nm, over the central xz -plane of the 50 μm -thick PhC cell with 80 – 40 – 20 SiO_2 - SiN_x - Al_2O_3 ARC. The slanted black lines (solid) correspond to the top surface of the silicon. The magnified view of a portion of the xz -plane shows in-plane Poynting vectors corresponding to the slow photonic modes.

parallel-to-interface and vortex-like flow of light. These modes, beyond the realm of ray-optics, lead to long dwell-time of photons inside the PhC and high absorption of the long-wavelength light.

Funding. Science and Engineering Research Board (SRG/2021/001777); Ontario Research Foundation (506441).

Disclosures. The authors declare no conflicts of interest.

Data availability. Data underlying the results presented in this paper are not publicly available at this time but may be obtained from the authors upon reasonable request.

References

1. M. A. Green, E. D. Dunlop, M. Yoshita, *et al.*, "Solar cell efficiency tables (version 62)," *Prog. Photovoltaics* **31**(7), 651–663 (2023).
2. M. Powalla, S. Paetel, E. Ahlswede, *et al.*, "Thin-film solar cells exceeding 22% solar cell efficiency: An overview on CdTe-, Cu(In,Ga)Se₂-, and perovskite-based materials," *Appl. Phys. Rev.* **5**(4), 041602 (2018).
3. P. Sinha and A. Wade, "Addressing Hotspots in the Product Environmental Footprint of CdTe Photovoltaics," *IEEE J. Photovoltaics* **8**, 793 (2018).
4. J. Ramanujam and U. P. Singh, "Copper Indium gallium selenide based solar cells-a review," *Energy Environ. Sci.* **10**(6), 1306–1319 (2017).
5. J. Zhao, A. Wang, and M. A. Green, "24.5% Efficiency Silicon PERT Cells on MCZ Substrates and 24.7% Efficiency PERL Cells on FZ Substrates," *Prog. Photovoltaics* **7**(6), 471–474 (1999).
6. M. A. Green, "The Path to 25% Silicon Solar Cell Efficiency: History of Silicon Cell Evolution," *Prog. Photovoltaics* **17**(3), 183–189 (2009).
7. F. Haase, C. Hollemann, S. Schafer, *et al.*, "Laser contact openings for local poly-Si-metal contacts enabling 26.1%-efficient POLO-IBC solar cells," *Solar Energy Materials and Solar Cells* **186**, 184–193 (2018).
8. C. Hollemann, F. Haase, S. Schafer, *et al.*, "26.1%-efficient POLO-IBC cells: Quantification of electrical and optical loss mechanisms," *Prog. Photovoltaics* **27**(11), 950–958 (2019).
9. K. Yoshikawa, H. Kawasaki, W. Yoshida, *et al.*, "Silicon Heterojunction solar cell with interdigitated back contacts for a photoconversion efficiency over 26%," *Nat. Energy* **2**(5), 17032 (2017).
10. H. Lin, M. Yang, X. Ru, *et al.*, "Silicon heterojunction solar cells with up to 26.8% efficiency achieved by electrically optimized nanocrystalline-silicon hole contact layers," *Nat. Energy* **8**(8), 789–799 (2023).
11. NREL: interactive best research cell efficiency chart: <https://www.nrel.gov/pv/interactive-cell-efficiency.html>.
12. T. Tiedje, E. Yablonovitch, G. Cody, *et al.*, "Limiting efficiency of silicon solar cells," *IEEE Trans. on Electron Devices* **31**(5), 711–716 (1984).
13. A. Ingenito, O. Isabella, and M. Zeman, "Experimental demonstration of $4n^2$ classical absorption limit in nanotextured ultrathin solar cells with dielectric omnidirectional back reflector," *ACS Photonics* **1**(3), 270–278 (2014).
14. A. Richter, M. Hermle, and S. W. Glunz, "Reassessment of the limiting efficiency for crystalline silicon solar cells," *IEEE J. Photovoltaics* **3**(4), 1184–1191 (2013).
15. S. John, "Strong localization of photons in certain disordered dielectric superlattices," *Phys. Rev. Lett.* **58**(23), 2486–2489 (1987).
16. E. Yablonovitch, "Inhibited spontaneous emission in solid-state physics and electronics," *Phys. Rev. Lett.* **58**(20), 2059–2062 (1987).
17. S. Bhattacharya and S. John, "Beyond 30% conversion efficiency in silicon solar cells: A numerical demonstration," *Sci. Rep.* **9**(1), 12482 (2019).
18. S. Bhattacharya and S. John, "Photonic crystal light trapping: Beyond 30% conversion efficiency for silicon photovoltaics," *APL Photonics* **5**(2), 020902 (2020).
19. S. Eyderman, S. John, and A. Deinega, "Solar light trapping in slanted conical-pore photonic crystals: Beyond statistical ray trapping," *J. Appl. Phys.* **113**(15), 154315 (2013).
20. S. Bhattacharya, I. Baydoun, M. Lin, *et al.*, "Towards 30% power conversion efficiency in thin-silicon photonic crystal solar cells," *Phys. Rev. Appl.* **11**(1), 014005 (2019).
21. B. Tian, X. Zheng, T. J. Kempa, *et al.*, "Coaxial silicon nanowires as solar cells and nanoelectronic power sources," *Nature* **449**(7164), 885–889 (2007).
22. L. Tsakalakos, J. Balch, J. Fronheiser, *et al.*, "Silicon nanowire solar cells," *Appl. Phys. Lett.* **91**(23), 233117 (2007).
23. T. Stelzner, M. Pietsch, G. Andrea, *et al.*, "Silicon nanowire-based solar cells," *Nanotechnology* **19**(29), 295203 (2008).
24. J. Li, H. Yu, S. M. Wong, *et al.*, "Si nanopillar array optimization on Si thin films for solar energy harvesting," *Appl. Phys. Lett.* **95**(3), 033102 (2009).
25. A. Kandalala, T. Betti, and A. Fontcuberta, "General theoretical considerations on nanowire solar cell designs," *Phys. Status Solidi A* **206**(1), 173–178 (2009).
26. E. Garnett and P. Yang, "Light Trapping in Silicon Nanowire Solar Cells," *Nano Lett.* **10**(3), 1082–1087 (2010).
27. G. Demsey and S. John, "Solar energy trapping with modulated silicon nanowire photonic crystals," *J. Appl. Phys.* **112**(7), 074326 (2012).

28. A. Deinega and S. John, "Solar power conversion efficiency in modulated silicon nanowire photonic crystals," *J. Appl. Phys.* **112**(7), 074327 (2012).
29. A. Deinega, S. Eyderman, and S. John, "Coupled optical and electrical modeling of solar cell based on conical pore silicon photonic crystals," *J. Appl. Phys.* **113**(22), 224501 (2013).
30. A. Mavrokefalos, S. E. Han, S. Yerci, *et al.*, "Efficient Light Trapping in Inverted Nanopyramid Thin Crystalline Silicon Membranes for Solar Cell Applications," *Nano Lett.* **12**(6), 2792–2796 (2012).
31. S. Eyderman, S. John, M. Hafez, *et al.*, "Light-trapping optimization in wet-etched silicon photonic crystal solar cells," *J. Appl. Phys.* **118**(2), 023103 (2015).
32. M. S. Branham, W. Hsu, S. Yerci, *et al.*, "15.7% Efficient 10- μ m-Thick Crystalline Silicon Solar Cells Using Periodic Nanostructures," *Adv. Mater.* **27**, 2182–2188 (2015).
33. S. Foster and S. John, "Light-trapping design for thin-film silicon-perovskite tandem solar cells," *J. Appl. Phys.* **120**(10), 103103 (2016).
34. A. Mellor, I. Tobias, A. Marti, *et al.*, "Upper limits to absorption enhancement in thick solar cells using diffraction gratings," *Prog. Photovoltaics* **19**(6), 676–687 (2011).
35. J. Gjessing, A. S. Sudbo, and E. S. Marstein, "Comparison of periodic light-trapping structures in thin crystalline silicon solar cells," *J. Appl. Phys.* **110**(3), 033104 (2011).
36. R. Cariou, J. Benick, F. Feldmann, *et al.*, "III-V-on silicon solar cells reaching 33% photoconversion efficiency in two-terminal configuration," *Nat. Energy* **3**(4), 326–333 (2018).
37. Y. Park, E. Drouard, O. Daif, *et al.*, "Absorption enhancement using photonic crystals for silicon thin film solar cells," *Opt. Express* **17**(16), 14312 (2009).
38. S. El-Jallal, M. Hochedel, J. Capitolis, *et al.*, "Photonic crystal backbone for light trapping inside an ultrathin, low absorbing layer," *Opt. Express* **30**(16), 29694 (2022).
39. F. Berry, R. Mermet-Lyaudoz, J. M. Cuevas Davila, *et al.*, "Light management in Perovskite photovoltaic solar cells: A perspective," *Adv. Energy Mater.* **12**(20), 2200505 (2022).
40. A. Gaucher, A. Cattoni, C. Dupuis, *et al.*, "Ultrathin epitaxial silicon solar cells with inverted nanopyramid arrays for efficient light trapping," *Nano Lett.* **16**(9), 5358–5364 (2016).
41. P. Kuang, S. Eyderman, M. L. Hsieh, *et al.*, "Achieving an Accurate Surface Profile of a Photonic Crystal for Near-Unity Solar Absorption in a Super Thin-Film Architecture," *ACS Nano* **10**(6), 6116–6124 (2016).
42. S. Bhattacharya and S. John, "Designing high-efficiency thin silicon solar cells using parabolic-pore photonic crystals," *Phys. Rev. Appl.* **9**(4), 044009 (2018).
43. M. L. Hsieh, A. Kaiser, S. Bhattacharya, *et al.*, "Experimental demonstration of broadband solar absorption beyond the lambertian limit in certain thin silicon photonic crystals," *Sci. Rep.* **10**(1), 11857 (2020).
44. A. Chutinan and S. John, "Light trapping and absorption optimization in certain thin-film photonic crystal architectures," *Phys. Rev. A* **78**(2), 023825 (2008).
45. J. Maksimovic, J. Hu, S. H. Ng, *et al.*, "Beyond Lambertian light trapping for large-area silicon solar cells: fabrication methods," *Opto-Electron. Adv.* **5**(9), 210086 (2022).
46. J. Maksimovic, H. Mu, D. Smith, *et al.*, "Laser-patterned alumina mask and mask-less dry etch of si for light trapping with photonic crystal structures," *Micromachines* **14**(3), 550 (2023).
47. J. Maksimovic, H. Mu, M. Han, *et al.*, "Si-cr nano-alloys fabricated by direct femtosecond laser writing," *Materials* **16**(5), 1917 (2023).
48. EMTL: <http://fdtd.kintechlab.com/en/download>.
49. I. Valuev, A. Deinega, A. Knizhnik, *et al.*, "Creating Numerically Efficient FDTD Simulations Using Generic C++ Programming," *Lecture Notes in Computer Science* **4707**, 213–226 (2007).
50. A. Taflove and S. C. Hagness, *Computational Electrodynamics: The Finite Difference Time-Domain Method*, (Artech House, Boston, 2005).
51. A. Deinega and S. John, "Effective optical response of silicon to sunlight in the finite-difference time-domain method," *Opt. Lett.* **37**(1), 112 (2012).
52. H. Cui, P. R. Campbell, and M. A. Green, "Optimisation of the back surface reflector for textured polycrystalline Si thin film solar cells," *Energy Procedia* **33**, 118–128 (2013).
53. M. A. Green and M. Keevers, "Optical properties of intrinsic silicon at 300 K," *Prog. Photovoltaics* **3**(3), 189–192 (1995).
54. A. Ingenito, O. Isabella, and M. Zeman, "Nano-cones on micro-pyramids: modulated surface textures for maximal spectral response and high-efficiency solar cells," *Prog. Photovoltaics* **23**(11), 1649–1659 (2015).
55. C. Schinke, P. C. Pees, J. Schmidt, *et al.*, "Uncertainty analysis for the coefficient of band-to-band absorption of crystalline silicon," *AIP Adv.* **5**(6), 067168 (2015).
56. Fitting of dielectric function, <http://fdtd.kintechlab.com/en/fitting>.
57. K. Q. Le and S. John, "Synergistic plasmonic and photonic crystal lighttrapping: Architectures for optical upconversion in thin-film solar cells," *Opt. Express* **22**(S1), A1 (2014).